Mueller matrix imaging ellipsometry for nanostructure metrology

Shiyuan Liu,[1,2] Weichao Du,[2] Xiuguo Chen,[2,*] Hao Jiang,[1] and Chuanwei Zhang[1]

[1] *State Key Laboratory of Digital Manufacturing Equipment and Technology, Huazhong University of Science and Technology, Wuhan 430074, China*

[2] *Wuhan National Laboratory for Optoelectronics, Huazhong University of Science and Technology, Wuhan 430074, China*

*[*xiuguochen@hust.edu.cn](mailto:xiuguochen@hust.edu.cn)*

Abstract: In order to achieve effective process control, fast, inexpensive, nondestructive and reliable nanometer scale feature measurements are extremely useful in high-volume nanomanufacturing. Among the possible techniques, optical scatterometry is relatively ideal due to its high throughput, low cost, and minimal sample damage. However, this technique is inherently limited by the illumination spot size of the instrument and the low efficiency in construction of a map of the sample over a wide area. Aiming at these issues, we introduce conventional imaging techniques to optical scatterometry and combine them with Mueller matrix ellipsometry based scatterometry, which is expected to be a powerful tool for the measurement of nanostructures in future high-volume nanomanufacturing, and propose to apply Mueller matrix imaging ellipsometry (MMIE) for nanostructure metrology. Two kinds of nanostructures were measured using an in-house developed Mueller matrix imaging ellipsometer in this work. The experimental results demonstrate that we can achieve Mueller matrix measurement and analysis for nanostructures with pixel-sized illumination spots by using MMIE. We can also efficiently construct parameter maps of the nanostructures over a wide area with pixel-sized lateral resolution by performing parallel ellipsometric analysis for all the pixels of interest.

©2015 Optical Society of America

OCIS codes: (120.0120) Instrumentation, measurement, and metrology; (120.2130) Ellipsometry and polarimetry; (110.0110) Imaging systems; (290.3200) Inverse scattering; (050.1950) Diffraction gratings.

References and links

1. C. J. Raymond, "Scatterometry for semiconductor metrology," in *Handbook of Silicon Semiconductor Metrology*, A. C. Diebold, ed. (CRC, 2001), Chap. 18, pp. 477–514.
2. B. Bunday, T. A. Germer, V. Vartanian, A. Cordes, A. Cepler, and C. Settens, "Gaps analysis for CD metrology beyond the 22 nm node," Proc. SPIE **8681**, 86813B (2013).
3. T T. Novikova, A. De Martino, S. B. Hatit, and B. Drévillon, "Application of Mueller polarimetry in conical diffraction for critical dimension measurements in microelectronics," Appl. Opt. **45**(16), 3688–3697 (2006).
4. T. Novikova, A. De Martino, P. Bulkin, Q. Nguyen, B. Drévillon, V. Popov, and A. Chumakov, "Metrology of replicated diffractive optics with Mueller polarimetry in conical diffraction," Opt. Express **15**(5), 2033–2046 (2007).
5. Y. N. Kim, J. S. Paek, S. Rabello, S. Lee, J. Hu, Z. Liu, Y. Hao, and W. McGahan, "Device based in-chip critical dimension and overlay metrology," Opt. Express **17**(23), 21336–21343 (2009).
6. X. G. Chen, S. Y. Liu, C. W. Zhang, and H. Jiang, "Measurement configuration optimization for accurate grating reconstruction by Mueller matrix polarimetry," J. Micro/Nanolithogr., MEMS, MOEMS **12**(3), 033013 (2013).
7. X. G. Chen, C. W. Zhang, and S. Y. Liu, "Depolarization effects from nanoimprinted grating structures as measured by Mueller matrix polarimetry," Appl. Phys. Lett. **103**(15), 151605 (2013).
8. X. Chen, S. Liu, C. Zhang, H. Jiang, Z. Ma, T. Sun, and Z. Xu, "Accurate characterization of nanoimprinted resist patterns using Mueller matrix ellipsometry," Opt. Express **22**(12), 15165–15177 (2014).
9. X. G. Chen, C. W. Zhang, S. Y. Liu, H. Jiang, Z. C. Ma, and Z. M. Xu, "Mueller matrix ellipsometric detection of profile asymmetry in nanoimprinted grating structures," J. Appl. Phys. **116**(19), 194305 (2014).
10. R. M. Silver, T. A. Germer, R. Attota, B. M. Barnes, B. Bunday, J. Allgair, E. Marx, and J. Jun, "Fundamental limits of optical critical dimension metrology: a simulation study," Proc. SPIE **6518**, 65180U (2007).

#239998 Received 28 Apr 2015; revised 18 Jun 2015; accepted 22 Jun 2015; published 24 Jun 2015

11. M. Losurdo, M. Bergmair, G. Bruno, D. Cattelan, C. Cobet, A. de Martino, K. Fleischer, Z. Dohcevic-Mitrovic, N. Esser, M. Galliet, R. Gajic, D. Hemzal, K. Hingerl, J. Humlicek, R. Ossikovski, Z. V. Popovic, and O. Saxl, "Spectroscopic ellipsometry and polarimetry for materials and systems analysis at the nanometer scale: state-of-the-art, potential, and perspectives," J. Nanopart. Res. **11**(7), 1521–1554 (2009).
12. C. Fallet, T. Novikova, M. Foldyna, S. Manhas, B. Haj Ibrahim, A. De Martino, C. Vannuffel, and C. Constancias, "Overlay measurements by Mueller polarimetry in back focal plane," J. Micro/Nanolithogr., MEMS, MOEMS **10**(3), 033017 (2011).
13. G. Jin, R. Jansson, and H. Arwin, "Imaging ellipsometry revisited: developments for visualization of thin transparent layers on silicon substrates," Rev. Sci. Instrum. **67**(8), 2930–2936 (1996).
14. U. Wurstbauer, C. Röling, U. Wurstbauer, W. Wegscheider, M. Vaupel, P. H. Thiesen, and D. Weiss, "Imaging ellipsometry of graphene," Appl. Phys. Lett. **97**(23), 231901 (2010).
15. A. Shan, M. Fried, G. Juhász, C. Major, O. Polgár, Á. Németh, P. Petrik, L. R. Dahal, J. Chen, Z. Huang, N. J. Podraza, and R. W. Collins, "High-speed imaging/mapping spectroscopic ellipsometry for in-line analysis of roll-to-roll thin-film photovoltaics," IEEE J. Photovoltaics **4**(1), 355–361 (2014).
16. R. W. Collins and J. Koh, "Dual rotating compensator multichannel ellipsometer: instrument design for real-time Mueller matrix spectroscopy of surfaces and films," J. Opt. Soc. Am. A **16**(8), 1997–2006 (1999).
17. W. C. Du, S. Y. Liu, C. W. Zhang, and X. G. Chen, "Optimal configurations for the dual rotating-compensator Mueller matrix ellipsometer," Proc. SPIE **8759**, 875925 (2013).
18. C. H. Herzinger, B. Johs, W. A. McGahan, J. A. Woollam, and W. Paulson, "Ellipsometric determination of optical constants for silicon and thermally grown silicon dioxide via a multi-sample, multi-wavelength, multi-angle investigation," J. Appl. Phys. **83**(6), 3323–3336 (1998).
19. E. D. Palik, *Handbook of Optical Constants of Solids* (Academic, 1991).
20. M. G. Moharam, E. B. Grann, D. A. Pommet, and T. K. Gaylord, "Formulation for stable and efficient implementation of the rigorous coupled-wave analysis of binary gratings," J. Opt. Soc. Am. A **12**(5), 1068–1076 (1995).
21. L. Li, "New formulation of the Fourier modal method for crossed surface-relief gratings," J. Opt. Soc. Am. A **14**(10), 2758–2767 (1997).
22. S. Y. Liu, Y. Ma, X. G. Chen, and C. W. Zhang, "Estimation of the convergence order of rigorous coupled-wave analysis for binary gratings in optical critical dimension metrology," Opt. Eng. **51**(8), 081504 (2012).
23. R. M. A. Azzam and N. M. Bashara, *Ellipsometry and Polarized Light* (North-Holland, 1977).
24. J. Zhu, S. Liu, X. Chen, C. Zhang, and H. Jiang, "Robust solution to the inverse problem in optical scatterometry," Opt. Express **22**(18), 22031–22042 (2014).
25. X. Chen, S. Liu, C. Zhang, and H. Jiang, "Improved measurement accuracy in optical scatterometry using correction-based library search," Appl. Opt. **52**(27), 6726–6734 (2013).
26. X. G. Chen, S. Y. Liu, H. G. Gu, and C. W. Zhang, "Formulation of error propagation and estimation in grating reconstruction by a dual-rotating compensator Mueller matrix polarimeter," Thin Solid Films **571**, 653–659 (2014).
27. J. J. Gil and E. Bernabeu, "Depolarization and polarization indices of an optical system," Opt. Acta (Lond.) **33**(2), 185–189 (1986).

1. Introduction

Nanomanufacturing is referred to as the manufacturing of products with feature dimensions at the nanometer scale. It is an essential bridge between the newest discoveries of fundamental nanoscience and real-world nanotechnology-enabled products. One critical issue to realize nanomanufacturing is the development of necessary instrumentation and metrology at the nanoscale, especially the fast, low-cost, and non-destructive metrology techniques that are suitable in high-volume nanomanufacturing. The currently available metrology tools, such as scanning electron microscopy (SEM), atomic force microscopy (AFM), or transmission electron microscopy (TEM), are mostly suitable for the exploratory nanoscale research while are not capable of meeting the metrology requirements in high-volume nanomanufacturing. In comparison, optics-based metrology tools have drawn more and more attention in semiconductor manufacturing because of their attractive merits, such as low cost, noncontact, non-destruction, and high throughput. As a non-imaging technique, optical scatterometry has been introduced for critical dimension (CD) and overlay metrology with great success for many years.

The optical scatterometry involves an inverse diffraction problem solving process with the objective of finding a structural profile whose theoretical signature can best match the measured one [1]. Despite the great success for the CD and overlay metrology, conventional optical scatterometry, which is traditionally based on reflectometry and ellipsometry, is quickly reaching its limit and requires improvements for future process nodes with the ever-decreasing in feature dimensions [2]. Compared with conventional optical scatterometry, which at most obtains two ellipsometric angles, Mueller matrix ellipsometry (MME),

#239998 Received 28 Apr 2015; revised 18 Jun 2015; accepted 22 Jun 2015; published 24 Jun 2015
© 2015 OSA

sometimes also referred to as Mueller matrix polarimetry, can provide up to 16 quantities of a 4 × 4 Mueller matrix in each measurement. Consequently, MME-based scatterometry can acquire much more useful information about the sample and can achieve better measurement sensitivity and accuracy [3–9], and is thereby expected to be a powerful tool for nanostructure metrology in the future high-volume nanomanufacturing.

From the fundamental measurement mechanism, the above optical scatterometry techniques collect reflected light from the spot illuminated at the sample surface and deliver it to the detector system. The final reconstructed structural profiles are the averaged results over all structures confined in the illumination spot. In this sense, any sample structures smaller than the spot size will not be accurately discriminated. Particularly, when the sample is inhomogeneous, the above averaged analysis will lead to incorrect results. From another perspective, as the nanostructures on the chips are commonly aperiodic in reality, the scatterometric measurements are often made on special target gratings etched in scribe lines between the chips with an assumption that the dimensional characteristics of the target gratings are representative of those of the nanostructures themselves. With the continuous increase of integration scales of chips, the measurements would require much smaller targets than 50 μm × 50 μm gratings currently used in the scribe lines. In general, the size of the illumination spot should be smaller than that of the grating target and has a lower limit to cover at least several grating periods for the reflected fields to approach plane waves [10]. Smaller spot sizes are thereby required for accurate measurement of inhomogeneous samples as well as those small target gratings. Standard spot sizes are in the range from 3 to 1 mm in diameter, and microspot sizes are typically between 50 and 25 μm so far [11], depending on the spectral range of the measurement. Further smaller microspots will complicate the optical systems [12]. In addition, in order to construct a profile map of the sample, the optical scatterometry needs equipping a motorized stage and performs measurements spot-by-spot until enough data are collected. The final analysis efficiency and the lateral resolution of the constructed profile map are thus greatly limited.

Considering the great potential of MME as well as the inherent issues in scatterometry techniques, we combine MME with imaging techniques and propose to apply Mueller matrix imaging ellipsometry (MMIE) for grating reconstruction. Naturally, MMIE has all the characteristics of both MME and imaging techniques. First, MMIE can acquire a 4 × 4 imaging Mueller matrix in a single measurement. Each element of the imaging Mueller matrix is a two-dimensional image over the whole field of view, which allows for the direct visualization of the sample. According to the imaging Mueller matrix, we can intuitively choose the region of interest for further data analysis. Second, each pixel of the detector array in MMIE along with the front optical system is equivalent to a Mueller matrix ellipsometer in principle. Moreover, this equivalent Mueller matrix ellipsometer has a pixel-sized illumination spot, which is much smaller than the microspot in scatterometry techniques. In other word, a Mueller matrix imaging ellipsometer can be equivalently regarded as thousands of parallel-combined Mueller matrix ellipsometers with pixel-sized illumination spots. By applying MMIE, we can reconstruct grating structures by performing ellipsometric analysis for a single pixel of the detector array. We can also perform parallel ellipsometric analysis for multiple pixels of interest to construct a profile map of the sample over a wide area without scanning the sample stage. Consequently, the analysis efficiency and the lateral resolution of the constructed profile map will be greatly improved. To the best of our knowledge, except the characterization of film thickness uniformity [13–15], there is no reported study yet on the application of imaging ellipsometry techniques, especially MMIE, for nanostructure metrology.

The remainder of this paper is organized as follows. Section 2 first introduces the principle and prototype of an in-house developed Mueller matrix imaging ellipsometer, and then introduces the grating samples measured by the instrument. Section 3 introduces the data analysis for grating reconstruction by MMIE, including the forward optical modeling, the inverse diffraction problem solving, as well as the measurement configuration optimization.

Section 4 provides the corresponding experimental results to demonstrate the great potential of MMIE for nanostructure metrology. Finally, we draw some conclusions in Section 5.

2. Experimental

2.1 Instrumentation of MMIE

A dual rotating-compensator configuration is adopted to measure the sample imaging Mueller matrices. As schematically shown in Fig. 1, an expanded parallel beam generated by a collimating lens illuminates a sample and the reflected light intensity is measured by a camera. The basic system layout of the dual rotating-compensator Mueller matrix imaging ellipsometer in order of light propagation is $PC_{r1}(\omega_1)SC_{r2}(\omega_2)A$, where P and A stand for the fixed polarizer and analyzer, C_{r1} and C_{r2} refer to the 1st and 2nd rotating compensators, and S stands for the sample. The 1st and 2nd compensators rotate synchronously at $\omega_1 = 5\omega$ and $\omega_2 = 3\omega$, where ω is the fundamental mechanical frequency. The Stokes vector $\mathbf{S}_{\text{out}}$ of the reflected light beam can be expressed as the following Mueller matrix product [8, 16]

$$\mathbf{S}_{\text{out}} = [\mathbf{M}_{\text{A}}\mathbf{R}(A)][\mathbf{R}(-C_2)\mathbf{M}_{\text{C2}}(\delta_2)\mathbf{R}(C_2)]\mathbf{M}_{\text{S}}[\mathbf{R}(-C_1)\mathbf{M}_{\text{C1}}(\delta_1)\mathbf{R}(C_1)][\mathbf{R}(-P)\mathbf{M}_{\text{P}}\mathbf{R}(P)]\mathbf{S}_{\text{in}}, \tag{1}$$

where $\mathbf{M}_i$ (i = P, A, C1, C2, S) is the Mueller matrix associated with each optical element and the sample. $\mathbf{R}(\alpha)$ is the Mueller rotation transformation matrix for rotation by the angle α, which can be the orientation angles of transmission axes of the polarizer and analyzer, P and A, and the orientation angles of fast axes of the 1st and 2nd rotating compensators, C_1 and C_2. Here, $C_1 = 5\omega t + C_{S1}$ and $C_2 = 3\omega t + C_{S2}$, and C_{S1} and C_{S2} represent the initial positions of the two compensators. δ_1 and δ_2 are the phase retardances of the 1st and 2nd compensators. The optimal values of P, A, C_{S1}, C_{S2}, δ_1 and δ_2 can be achieved using the optimization method presented in [17].

By multiplying the matrices in Eq. (1), we obtain the following expression for the irradiance at the detector (proportional to the first element of $\mathbf{S}_{\text{out}}$)

$$\begin{aligned} I(t) &= I_{00}M_{11}\left\{a_0 + \sum_{n=1}^{16}\left[a_{2n}\cos(2n\omega t - \phi_{2n}) + b_{2n}\sin(2n\omega t - \phi_{2n})\right]\right\} \\ &= I_0\left\{1 + \sum_{n=1}^{16}\left[\alpha_{2n}\cos(2n\omega t - \phi_{2n}) + \beta_{2n}\sin(2n\omega t - \phi_{2n})\right]\right\}, \end{aligned} \tag{2}$$

where I_{00} is the spectral response function and ϕ_{2n} is the angular phase shift. $I_0 = I_{00}M_{11}a_0$, $\alpha_{2n} = a_{2n}/a_0$, and $\beta_{2n} = b_{2n}/a_0$ are the d.c. and d.c.-normalized a.c. harmonic coefficients, respectively. The sample Mueller matrix elements M_{ij} (i, j = 1, 2, 3, 4) are linear combinations of α_{2n} and β_{2n}. By performing Fourier analysis, the sample Mueller matrix elements associated with each pixel of the camera can be extracted from these harmonic coefficients [16].

According to the above measurement principle, we developed a prototype of the Mueller matrix imaging ellipsometer, as depicted in Fig. 1, based on the previously developed dual rotating-compensator Mueller matrix ellipsometer in our lab [8]. The light source is a laser-driven light source with fiber-coupled output (LDLS$^{\text{TM}}$ Eq. (-99)FC, Energetiq, USA). The wavelength of the probe light is chosen by a monochromator (Omni-λ320, Zolix, China). The imaging lens is a matched achromatic doublet pair with an image magnification of 1:1 (MAP10100100-A, Thorlabs, USA). The camera is a high speed and high sensitive sCMOS camera with a pixel size of 6.5 μm × 6.5 μm and a sustained frame rate of 100 fps (Zyla 5.5 sCMOS, Andor, UK). The camera was mounted with a slight tilt as shown in Fig. 1 in order to obtain a clear image of the sample surface [13]. The two arms of the instrument and the sample stage can be rotated to change the incidence and azimuthal angles in experiments.

#239998 Received 28 Apr 2015; revised 18 Jun 2015; accepted 22 Jun 2015; published 24 Jun 2015
© 2015 OSA

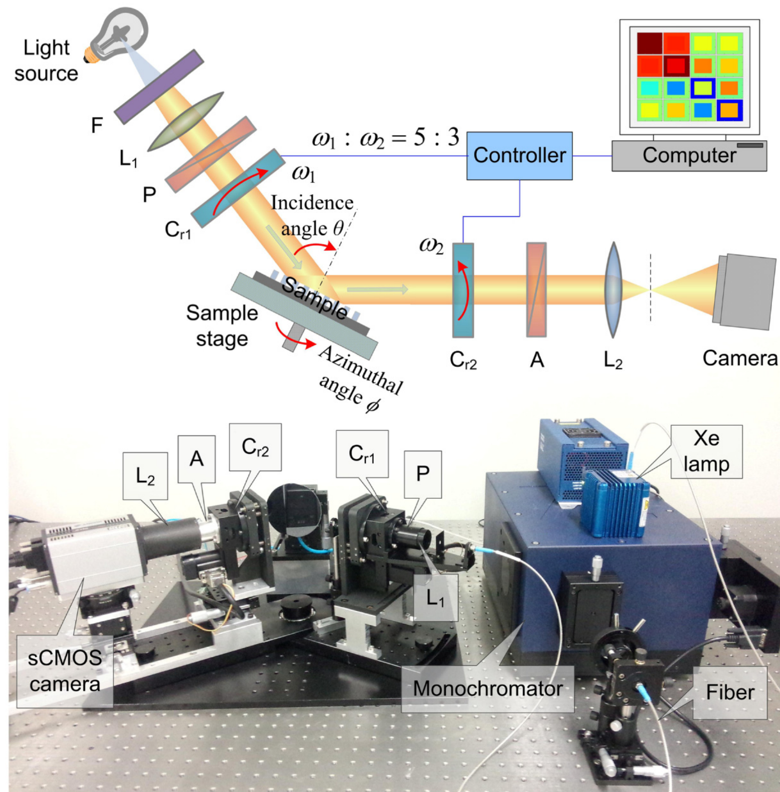

Fig. 1. Scheme (top) and prototype (bottom) of the dual rotating-compensator Mueller matrix imaging ellipsometer. L_1 and L_2, collimating lens and imaging lens; F, filter or monochromator; P and A, polarizer and analyzer; C_{r1} and C_{r2}, the 1st and 2nd rotating compensator.

2.2 Sample description

Two kinds of grating structures were measured using the in-house developed Mueller matrix imaging ellipsometer. One is a Si grating structure that was fabricated by e-beam lithography followed by dry etching and was used as a template in nanoimprint lithography [7–9]. The Si grating structure is in a rectangular region with a size of about 750 μm × 1800 μm, which is located in the middle of the whole Si wafer and is also termed as the metrological box in the remainder of this paper. Figure 2(a) shows the SEM micrograph of the investigated Si grating template, which has a pitch of 800 nm. As shown in Fig. 2(a), the Si grating structure is characterized by top CD x_1, grating height x_2, and sidewall angle x_3. In the data analysis, we fixed the grating pitch and just let the parameters x_1~x_3 vary. The optical constants of Si were fixed at values taken from [18]. Another sample is a typical etched trench nanostructure from the practical manufacturing process lines of flash memory storage cells. Flash memory is an electronic non-volatile computer storage medium that can be electrically erased reprogrammed. Due to the much lower cost than byte-programmable EEPROM (electrically erasable programmable read-only memory), flash memory has become the dominant memory type wherever a system requires a significant amount of non-volatile, solid state storage. The key of flash memory is its storage cells, which are usually comprised of some nanostructures. The investigated etched trench nanostructure was made on a 12 inch Si wafer that consists of thousands of dies and each die has a size of about 280 μm × 1200 μm. Figure 2(b) depicts the TEM micrograph of the etched trench nanostructure, which has a pitch of 154 nm. As shown in Fig. 2(b), the etched trench nanostructure has three grating layers. The Si_3N_4 grating layer is characterized by top CD x_1, grating height x_2, and bottom CD x_3. The SiO_2 grating layer has

#239998 Received 28 Apr 2015; revised 18 Jun 2015; accepted 22 Jun 2015; published 24 Jun 2015
© 2015 OSA

the same sidewall angle with that of the Si_3N_4 grating layer and is characterized by top CD x_3 and grating height x_4. The Si grating layer has a different sidewall angle to that of the former two grating layers and is characterized by grating height x_5 and bottom CD x_6. In the data analysis, we fixed the grating pitch and just let the parameters x_1~x_6 vary. The optical constants of Si_3N_4 and SiO_2 were fixed at values taken from [19].

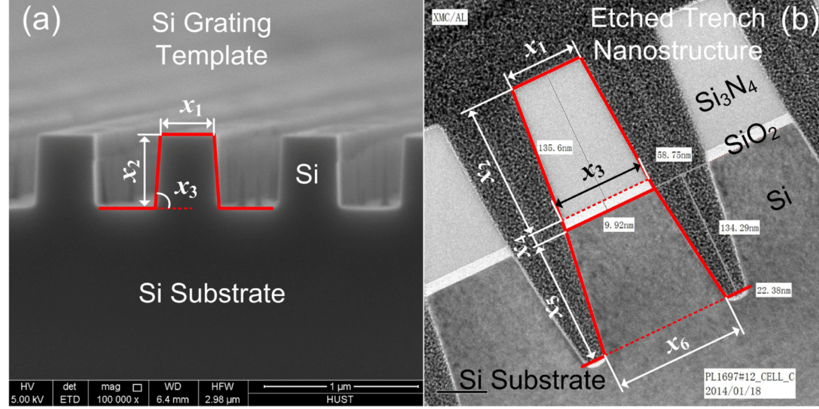

Fig. 2. SEM/TEM micrographs and geometric models of the Si grating template and etched trench nanostructure.

3. Theory

As schematically shown in Fig. 3, without loss of generality, we denote the structural parameters under measurement as a P-dimensional vector $\mathbf{x} = [x_1, x_2, \ldots, x_P]^{\mathrm{T}}$, where $x_1, x_2, \ldots, x_P$ can be the line width, line height, and sidewall angle of the grating sample, and the superscript "T" represents the transpose. The vector $\mathbf{a} = [\lambda, \theta, \phi]^{\mathrm{T}}$ that consists of the selected wavelengths λ, incidence angles θ, and azimuthal angles ϕ denotes the measurement configuration. Theoretical Mueller matrices of a grating sample can be calculated by rigorous coupled-wave analysis (RCWA) [20–22]. In RCWA, both the permittivity function and electromagnetic fields are expanded into Fourier series. Afterwards, the tangential field components are matched at boundaries between different layers, and thereby the boundary-value problem is reduced to an algebraic eigenvalue problem. The overall reflection coefficients are calculated by solving this eigenvalue problem. According to the reflection coefficients, the 2 × 2 Jones matrix $\mathbf{J}(\mathbf{x}, \mathbf{a})$ associated with the zeroth order reflected light of the grating sample, which connects the incoming Jones vector with the reflected Jones vector, can be formulated by

$$\begin{bmatrix} E_{\mathrm{rp}} \\ E_{\mathrm{rs}} \end{bmatrix} = \mathbf{J}(\mathbf{x}, \mathbf{a}) \begin{bmatrix} E_{\mathrm{ip}} \\ E_{\mathrm{is}} \end{bmatrix} = \begin{bmatrix} r_{\mathrm{pp}} & r_{\mathrm{ps}} \\ r_{\mathrm{sp}} & r_{\mathrm{ss}} \end{bmatrix} \begin{bmatrix} E_{\mathrm{ip}} \\ E_{\mathrm{is}} \end{bmatrix}, \tag{3}$$

where $E_{\mathrm{s,p}}$ refers to the electric field component perpendicular and parallel to the plane of incidence, respectively. In the absence of depolarization, the 4 × 4 Mueller matrix $\mathbf{M}(\mathbf{x}, \mathbf{a})$ can be calculated from the Jones matrix $\mathbf{J}(\mathbf{x}, \mathbf{a})$ by [23]

$$\mathbf{M}(\mathbf{x},\mathbf{a}) = \begin{bmatrix} M_{11} & M_{12} & M_{13} & M_{14} \\ M_{21} & M_{22} & M_{23} & M_{24} \\ M_{31} & M_{32} & M_{33} & M_{34} \\ M_{41} & M_{42} & M_{43} & M_{44} \end{bmatrix} = \mathbf{A}\left[\mathbf{J}(\mathbf{x},\mathbf{a}) \otimes \mathbf{J}^*(\mathbf{x},\mathbf{a})\right]\mathbf{A}^{-1}, \tag{4a}$$

where the symbol ⊗ denotes the Kronecker product, $\mathbf{J}^*(\mathbf{x}, \mathbf{a})$ is the complex conjugate of $\mathbf{J}(\mathbf{x}, \mathbf{a})$, and the matrix $\mathbf{A}$ is given by

#239998 Received 28 Apr 2015; revised 18 Jun 2015; accepted 22 Jun 2015; published 24 Jun 2015
© 2015 OSA

$$\mathbf{A}=\begin{bmatrix}1&0&0&1\\1&0&0&-1\\0&1&1&0\\0&\mathrm{i}&-\mathrm{i}&0\end{bmatrix}. \tag{4b}$$

In practice, the Mueller matrix $\mathbf{M}(\mathbf{x}, \mathbf{a})$ is usually normalized to the (1, 1)th element M_{11}, with the normalized Mueller matrix elements $m_{ij} = M_{ij}/M_{11}$.

The least-squares regression analysis is then performed for any pixel of the camera of MMIE, during which the fitting parameters are varied until the calculated and measured data match as close as possible [24]. Alternatively, the library search can also be performed, during which a Mueller matrix spectra library is generated offline prior to the experiment and then the library is searched to find the best match with the measured spectra [25]. In both of the above approaches, the solution of the fitting parameters is achieved by minimizing a weighted mean square error function defined by

$$\chi_r^2=\frac{1}{15N-P}\sum_{k=1}^{N}\sum_{i,j=1}^{4}\left[\frac{m_{ij,k}^{\text{meas}}-m_{ij,k}^{\text{calc}}(\mathbf{x},\mathbf{a})}{\sigma(m_{ij,k})}\right]^2, \tag{5}$$

where k indicates the k-th spectral point from the total number N, indices i and j show all the Mueller matrix elements except m_{11}, and P is the total number of fitting parameters. $m_{ij,k}^{\text{meas}}$ denotes the Mueller matrix elements collected by the selected pixel of the camera, and $m_{ij,k}^{\text{calc}}(\mathbf{x}, \mathbf{a})$ denotes the calculated Mueller matrix elements associated with the parameter vector $\mathbf{x}$ and the configuration vector $\mathbf{a}$. Since the wavelengths λ are varied in a spectral range, here the vector $\mathbf{a}$ is only the combination of the fixed incidence and azimuthal angles, i.e., $\mathbf{a} = [\theta, \phi]^{\mathrm{T}}$. $\sigma(m_{ij,k})$ is the estimated standard deviation associated with $m_{ij,k}$. The fitting procedure also delivers 95% confidence limits for the fitting parameters. The confidence limits are defined as $1.96\times\chi_r\times\sqrt{C_{ii}}$, where C_{ii} is the ith diagonal element of the fitting parameter covariance matrix [26].

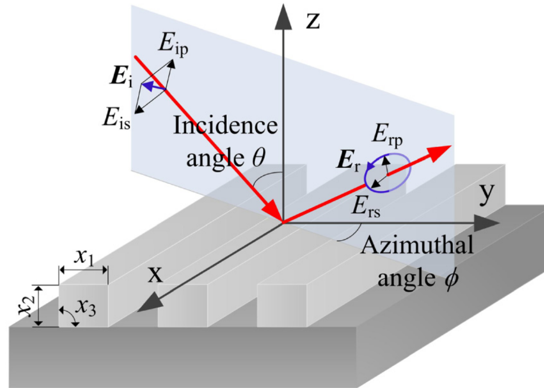

Fig. 3. Representation of polarized light incidence for a one-dimensional grating structure.

Similar to MME, we can also obtain different measurement configurations by changing the combination of incidence and azimuthal angles in MMIE. As revealed in the previous literatures [3, 6], the solution accuracy of the fitting parameters sometimes varies greatly in different measurement configurations. To find the optimal configuration, with which more accurate measurement can be achieved, we can perform the following optimization by [6, 8]

#239998 Received 28 Apr 2015; revised 18 Jun 2015; accepted 22 Jun 2015; published 24 Jun 2015
© 2015 OSA

$$\left(\theta_{\text{opt}}, \phi_{\text{opt}}\right) = \arg \min_{\theta\in\Theta,\, \phi\in\Phi} \left[\max_{\mathbf{x}\in\Omega} \left(\left\| \tilde{\mathbf{J}}_{\mathbf{x}}^{+} \tilde{\mathbf{J}}_{\mathbf{a}} \right\| \right) \right], \tag{6}$$

where $\tilde{\mathbf{J}}_{\mathbf{x}}^{+} = \left(\tilde{\mathbf{J}}_{\mathbf{x}}^{\mathrm{T}} \tilde{\mathbf{J}}_{\mathbf{x}}\right)^{-1} \tilde{\mathbf{J}}_{\mathbf{x}}^{\mathrm{T}}$ is the Moore-Penrose pseudo-inverse of a weighted Jacobian matrix $\tilde{\mathbf{J}}_{\mathbf{x}}$ whose elements are proportional to partial derivatives of the Mueller matrix spectra with respect to elements in the parameter vector **x**. $\tilde{\mathbf{J}}_{\mathbf{a}}$ is also a weighted Jacobian matrix but with elements proportional to partial derivatives of the Mueller matrix spectra with respect to elements in the configuration vector $\mathbf{a} = [\theta, \phi]^{\mathrm{T}}$. The matrix $\tilde{\mathbf{J}}_{\mathbf{x}}^{+} \tilde{\mathbf{J}}_{\mathbf{a}}$ is referred to as the configuration error propagating matrix, and $\left\| \tilde{\mathbf{J}}_{\mathbf{x}}^{+} \tilde{\mathbf{J}}_{\mathbf{a}} \right\|$ describes the maximum gain factor in the propagation of the configuration error $\Delta\mathbf{a}$. In the optimization process, the values of $\left\| \tilde{\mathbf{J}}_{\mathbf{x}}^{+} \tilde{\mathbf{J}}_{\mathbf{a}} \right\|$ are firstly scanned in the given parameter domain Ω for the maximum. Then all of the maxima of $\left\| \tilde{\mathbf{J}}_{\mathbf{x}}^{+} \tilde{\mathbf{J}}_{\mathbf{a}} \right\|$ are scanned in the ranges of incidence and azimuthal angles (Θ and Φ) for the minimum. The combination of incidence and azimuthal angles corresponding to this minimum will be the final optimal measurement configuration.

It is also worth pointing out that the developed technique for nanostructure metrology is essentially identical to typical optical scatterometry techniques, in which only the zeroth order diffracted light of a periodic nanostructure is collected. In this sense, for a one-dimensional grating structure as depicted in Fig. 3 at a classical mounting (azimuthal angle $\phi = 0°$), the grating period Λ should satisfy that

$$\Lambda < \lambda \Big/ \left\{ \sin\left[\arcsin\left(NA\right) + \theta \right] - \sin\theta \right\}, \tag{7}$$

to avoid higher order diffracted light entering the camera. Here, NA represents the numerical aperture of the imaging lens shown in Fig. 1, which is less than 0.13 in our instrument. The above inequality is derived from the grating equation by assuming that the ambient of the grating is air. Since only the zeroth order diffracted light is collected, we actually cannot directly obtain the image of features of the grating structure. However, when the grating period Λ disobeys Eq. (7), higher order diffracted light will enter the camera and we will obtain the image of the grating structure. In this case, it is unnecessary to solve the inverse diffraction problem as described in Eq. (5) to extract the structural features, which can be directly obtained from the measured image by applying proper image reconstruction algorithms, as do in conventional image-based metrology techniques. It is therefore beyond the scope of this paper. In addition, to realize single-pixel ellipsometric analysis, the size of the illumination spot corresponding to a single pixel of the camera should cover several grating periods (at least 10 grating periods according to the simulation in [10]) for the diffracted electromagnetic fields to approach plane waves.

4. Results and discussion

The Si grating template and the etched trench nanostructure were then measured using the in-house developed Mueller matrix imaging ellipsometer. In the experiment, the spectral range was varied from 400 to 700 nm with increments of 10 nm. In order to reduce the calculation time of the optimization procedure described in Eq. (6), we fixed the incidence angle θ at 60° and only varied the azimuthal angle ϕ in a range from 0 to 90° with increments of 5° to find the optimal azimuthal configuration. The optimal azimuthal angle for the Si grating template was found to be at $\phi = 0°$ and at $\phi = 60°$ for the etched trench nanostructure, respectively. The standard deviation associated with the Mueller matrix elements $\sigma(m_{ij,k})$ in Eq. (5) was achieved based on the standard deviation of 30 repeat Mueller matrix measurements.

#239998 Received 28 Apr 2015; revised 18 Jun 2015; accepted 22 Jun 2015; published 24 Jun 2015
© 2015 OSA

4.1 Measurement of the Si grating template

As an example, Fig. 4 shows the measured imaging Mueller matrix at the wavelength of 500 nm. In MMIE, since each pixel of the camera together with the optical system before the camera can be regarded as a Mueller matrix ellipsometer in principle, we can thereby obtain a Mueller matrix at each wavelength from each pixel of the camera. All the Mueller matrices associated with each pixel of the camera compose the final imaging Mueller matrix. At the azimuthal angle of $\phi = 0°$, the two 2 × 2 off-diagonal blocks of the Mueller matrices of the Si grating template vanish, as can be observed from Fig. 4, and other matrix elements can be expressed in terms of conventional ellipsometric angles Ψ and Δ [23], i.e., $m_{12} = m_{21} = -\cos2\Psi$, $m_{34} = -m_{43} = \sin2\Psi\sin\Delta$, and $m_{33} = m_{44} = \sin2\Psi\cos\Delta$ ($m_{11} = m_{22} = 1$). According to Eq. (7), since only the zeroth order diffracted light of the Si grating is collected, we will not obtain the image of its structural features. However, due to the difference (or contrast) between the Mueller matrices associated with the Si substrate and the Si grating structure, we can readily distinguish the metrological box where the Si grating structure is from the measured imaging Mueller matrix given in Fig. 4. According to the imaging Mueller matrices, we can also intuitively choose the region or pixels of interest for further ellipsometric analysis to reconstruct the Si grating structure.

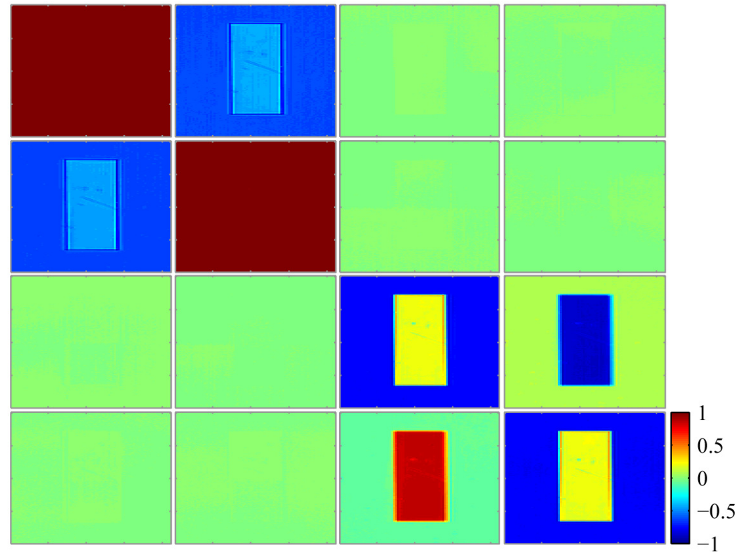

Fig. 4. The measured imaging Mueller matrix of the Si grating template at the wavelength of 500 nm. The middle rectangular region is the metrological box where the Si grating structure is, and other regions correspond to the Si substrate. The incidence and azimuthal angles are fixed at $\theta = 60°$ and $\phi = 0°$, respectively. The imaging Mueller matrix elements are normalized to m_{11}.

Table 1 presents the comparison of fitting parameters obtained from the SEM and MMIE measurements. We also provide the results measured by the previously developed dual rotating-compensator Mueller matrix ellipsometer in our lab with the same measurement configuration to that of MMIE. The developed Mueller matrix ellipsometer has a beam diameter of about 200 μm after equipping the focusing lens [8]. It is worth pointing out that the MMIE-measured results in Table 1 were extracted from the Mueller matrix spectra collected by a single pixel located near the center of the metrological box. In other word, the MMIE-measured results are equivalent to those obtained by a Mueller matrix ellipsometer with a beam size of about 6.5 μm × 6.5 μm. According to Table 1, we can observe that the MMIE-measured results exhibit good agreement with those measured by SEM and MME.

#239998 Received 28 Apr 2015; revised 18 Jun 2015; accepted 22 Jun 2015; published 24 Jun 2015
© 2015 OSA

Table 1. Comparison of fitting parameters of the Si grating template obtained from the MME, MMIE and SEM measurements.

Parameter	SEM	MME	MMIE[a]
x_1 [nm]	350	347.2 ± 0.77	348.9 ± 0.82
x_2 [nm]	472	469.1 ± 0.93	469.3 ± 1.01
x_3 [deg]	88	86.8 ± 0.10	87.1 ± 0.11

[a]The results were extracted from Mueller matrices collected by a single pixel of the camera

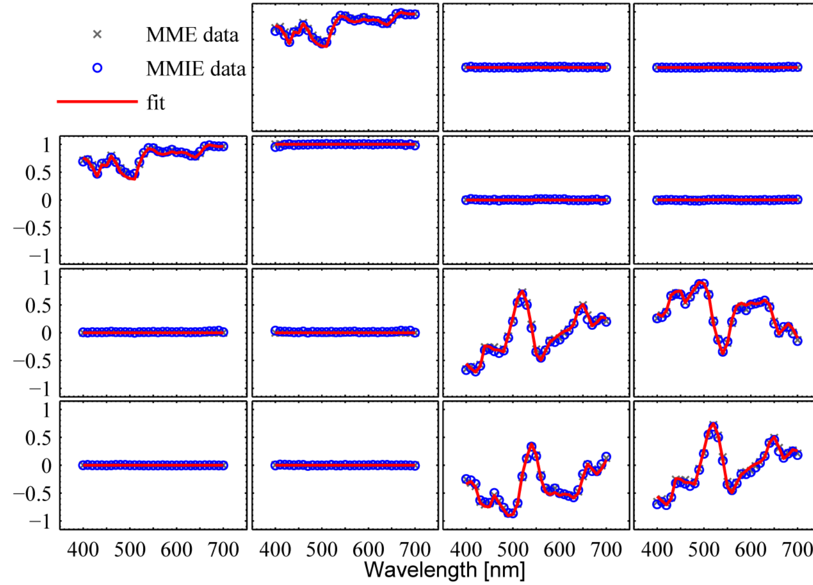

Fig. 5. Comparison of the measured Mueller matrix spectra of the Si grating template that were collected by MME and by a single pixel of the camera of MMIE as well as the calculated best-fit Mueller matrix spectra to the MMIE-measured Mueller matrix spectra. The wavelengths are varied from 400 to 700 nm with increments of 10 nm. The incidence and azimuthal angles are fixed at $\theta = 60°$ and $\phi = 0°$, respectively.

Figure 5 shows the comparison of Mueller matrix spectra measured by MME and MMIE at the corresponding pixel. As observed from Fig. 5, the MMIE-measured spectra exhibit good agreement with those measured by MME over most of the spectrum. The differences between them are mainly because that the MME- and MMIE-measured data are average values over different illumination locations and sizes. At an oblique incidence, an illumination spot with a radius of r will become an elliptic illumination spot with a minor axis (perpendicular to the plane of incidence) of r and a major axis (parallel to the plane of incidence) of $r/\cos\theta$. Hence, the MME data are the average over an elliptic illumination spot with a minor axis of about 200 μm and a major axis of about 400 μm, while the MMIE data are the average over a rectangular illumination spot with size of about 13 μm × 6.5 μm. According to the spot size, we can further know that, as for the MMIE measurement, the illumination spot covers at least 16 grating periods, which is sufficient for the reflected fields to approach plane waves. We also calculated the depolarization index spectrum associated with the MMIE-measured data by $DI = \sqrt{[\mathrm{Tr}(\mathbf{M}\mathbf{M}^{\mathrm{T}}) - M_{11}^2]/3M_{11}^2}$, $0 \le DI \le 1$ [27]. Here, $\mathrm{Tr}(\cdot)$ represents the matrix trace and $\mathbf{M}^{\mathrm{T}}$ is the transposed matrix of $\mathbf{M}$. $DI = 0$ and $DI = 1$ correspond to a totally depolarizing and totally non-depolarizing Mueller matrix, respectively. The calculated depolarization indices exhibited that $|DI - 1| < 0.025$ over the whole spectral range of 400~700 nm. The depolarization effect can thereby be ignored in the regression

#239998 Received 28 Apr 2015; revised 18 Jun 2015; accepted 22 Jun 2015; published 24 Jun 2015
© 2015 OSA

analysis. The calculated best-fit Mueller matrix spectra to the MMIE-measured spectra are presented in Fig. 5. A good match can be easily observed from Fig. 5, which yields of fitting error of $\chi_r^2 = 14.5$. The results shown in Table 1 and Fig. 5 thus reveal the potential of MMIE in realizing pixel-sized Mueller matrix measurement and analysis for the grating sample.

As shown in Fig. 4, we can obtain the Mueller matrices of the Si grating template over the whole field of view in a single measurement. Besides the ellipsometric analysis performed for a single pixel, we can also perform parallel ellipsometric analysis for all the pixels of interest located in the metrological box so as to obtain the variation of fitting parameters over a wide area. Figure 6 shows maps of the structural parameters x_1~x_3 of the Si grating template over the bottom half region of the metrological box. Since there are some contaminants on the surface of the Si grating sample outside this region, as can be observed from Fig. 4, we did not perform ellipsometric analysis for the entire metrological box. Additionally, to make sure that the illumination spot corresponding to each analyzed pixel covers identical and enough grating periods for the reflected fields to approach plane waves, we ignored 2 pixels located near the edges of the metrological box in the analysis, as presented in Fig. 6. The lateral resolution of Fig. 6 mainly depends on the pixel size of the camera, the image magnification of the imaging lens, and the incidence angle. For our instrument, the current lateral resolutions in the X and Y directions are about 13 μm and 6.5 μm, respectively. According to Fig. 6, we observe that there are several nanometer variations in the structural parameters of the Si grating template over the analyzed region. Nevertheless, the parameter maps exhibit relatively uniform variation and reasonable agreement with the corresponding result measured by SEM. In this sense, the result shown in Fig. 6 also explains why the fitting parameters measured by MME and MMIE presented in Table 1 show good agreement. Consequently, the result shown in Fig. 6 reveals the potential of MMIE in realizing parallel Mueller matrix measurement and analysis to construct maps of fitting parameters of grating structures over a wide area.

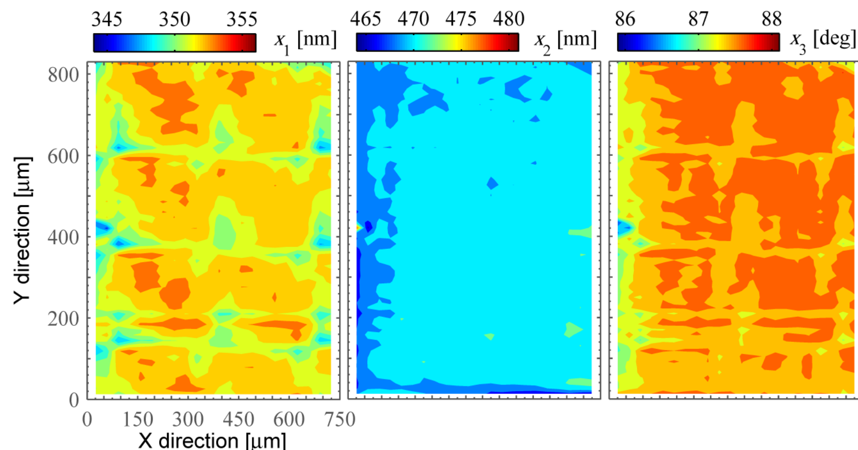

Fig. 6. Maps of the structural parameters x_1~x_3 of the Si grating template over the bottom half region of the metrological box shown in Fig. 4. The grating period is along the X direction. Data were obtained by performing ellipsometric analysis for each pixel of the measured imaging Mueller matrices. The measurement configuration is identical to that given in Fig. 5.

4.2 Measurement of the etched trench nanostructure

The etched trench sample from practical manufacturing process lines was also measured using the Mueller matrix imaging ellipsometer. Like the analysis for the Si grating template, as for the etched trench sample, we will first try to reconstruct the etched trench nanostructure from the Mueller matrices collected by a single pixel of the camera. Then, we will try to obtain the map of fitting parameters of the etched trench nanostructure over a whole die by performing ellipsometric analysis for each pixel of the measured imaging Mueller matrices.

#239998 Received 28 Apr 2015; revised 18 Jun 2015; accepted 22 Jun 2015; published 24 Jun 2015
© 2015 OSA

Table 2 presents the comparison of fitting parameters obtained from the TEM, MME and MMIE measurements. Here, the MMIE-measured results were extracted from the Mueller matrix spectra collected by a single pixel located near the center of a randomly selected die. According to Table 2, we can observe that the MMIE-measured results at the optimal azimuthal configuration of ϕ = 60° exhibit reasonable agreement with those measured by TEM and MME-measured results at the same configuration. We also compared the MMIE-measured results at ϕ = 60° with those obtained at ϕ = 0°. ϕ = 0° is the usual azimuthal configuration adopted in conventional (imaging) ellipsometry, because in this configuration the corresponding Mueller matrix elements can be fully expressed in terms of classical ellipsometric angles Ψ and Δ, which can thereby be entirely collected by conventional (imaging) ellipsometry. As can be observed from Table 2, except the parameter x_6, most of the other fitting parameters obtained at the optimal azimuthal configuration exhibit higher accuracy and moreover smaller uncertainties. Tables 3 and 4 present the parameter correlation coefficients obtained at ϕ = 0° and ϕ = 60°, respectively. The values of the parameter correlation coefficients fall between −1 and 1, with 0 meaning no correlation and with −1 and 1 meaning perfect correlation. It is noted from Tables 3 and 4 that the fitting parameters obtained at ϕ = 60° also have relatively smaller correlation than those obtained at ϕ = 0°. The results shown in Tables 2 to 4 therefore demonstrate the superiority of MMIE over conventional imaging ellipsometry.

Table 2. Comparison of fitting parameters of the etched trench nanostructure obtained from the MME, MMIE and TEM measurements.

Parameter	TEM	MME (ϕ = 60°)	MMIE[a]	
			ϕ = 60°	ϕ = 0°
x_1 [nm]	75.0	77.1 ± 0.88	74.5 ± 0.82	75.1 ± 3.53
x_2 [nm]	135.6	129.5 ± 2.44	133.8 ± 1.76	123.1 ± 10.63
x_3 [nm]	86.9	83.1 ± 0.88	81.9 ± 0.75	94.0 ± 0.73
x_4 [nm]	9.9	14.5 ± 2.45	12.9 ± 2.00	20.0. ± 6.17
x_5 [nm]	134.3	140.8 ± 1.18	140.4 ± 0.95	124.9 ± 1.21
x_6 [nm]	129.6	122.7 ± 0.64	121.7 ± 0.56	125.1 ± 0.60

[a]The results were extracted from Mueller matrices collected by a single pixel of the camera

Table 3. Parameter correlation coefficient matrix of the etched trench nanostructure obtained from the MMIE measurement at ϕ = 0°.

Parameter	x_1	x_2	x_3	x_4	x_5	x_6
x_1	1					
x_2	-0.899	1				
x_3	0.442	-0.360	1			
x_4	0.813	-0.981	0.322	1		
x_5	0.224	-0.056	-0.549	-0.016	1	
x_6	0.437	-0.536	-0.140	0.522	0.208	1

Table 4. Parameter correlation coefficient matrix of the etched trench nanostructure obtained from the MMIE measurement at ϕ = 60°.

Parameter	x_1	x_2	x_3	x_4	x_5	x_6
x_1	1					
x_2	0.200	1				
x_3	0.570	0.351	1			
x_4	-0.474	-0.944	-0.504	1		
x_5	-0.082	-0.053	-0.450	0.100	1	
x_6	-0.085	0.046	-0.239	-0.076	-0.229	1

#239998 Received 28 Apr 2015; revised 18 Jun 2015; accepted 22 Jun 2015; published 24 Jun 2015
© 2015 OSA

Figure 7 shows the comparison of the measured Mueller matrix spectra collected by MME and by the corresponding pixel of MMIE at ϕ = 60°. The MMIE-measured data exhibit reasonable agreement with those measured by MME. The differences between them as indicated in Fig. 7 are mainly due to the different measurement locations. We calculated the depolarization index spectrum associated with the MMIE-measured data. It was found that the calculated depolarization indices showed $|DI-1|<0.04$ over the whole spectral range of 400~700 nm. Hence, the depolarization effect can also be ignored in the regression analysis. Figure 7 presents the calculated best-fit Mueller matrix spectra to the MMIE-measured spectra. A good match can be easily observed from Fig. 7, which yields of fitting error of $\chi_r^2=11.7$.

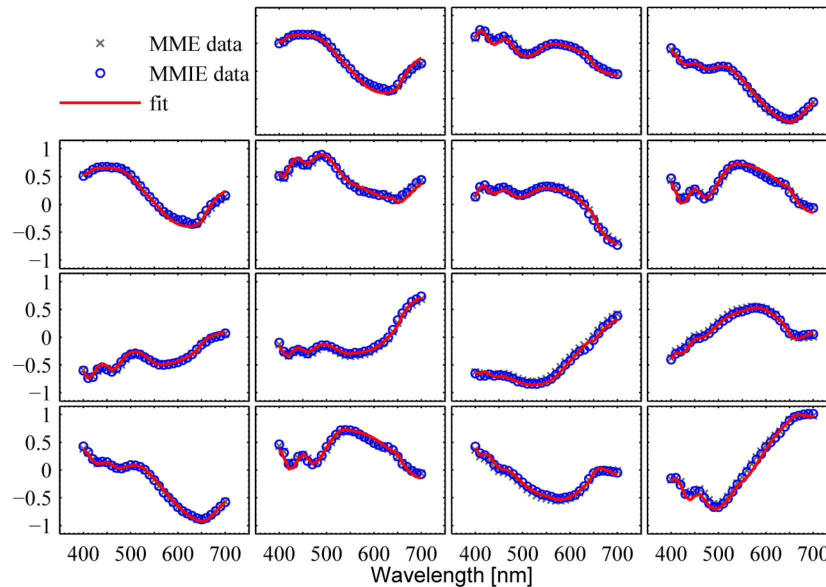

Fig. 7. Comparison of the measured Mueller matrix spectra of the etched trench nanostructure that were collected by MME and by a single pixel of the camera of MMIE as well as the calculated best-fit Mueller matrix spectra to the MMIE-measured Mueller matrix spectra. The wavelengths are varied from 400 to 700 nm with increments of 10 nm. The incidence and azimuthal angles are fixed at θ = 60° and ϕ = 60°, respectively.

We further performed parallel ellipsometric analysis at the optimal azimuthal configuration for all the pixels located in a randomly selected die to obtain the variation of fitting parameters over an entire die. Figure 8 presents maps of the structural parameters x_1~x_6 of the etched trench nanostructure over the selected die. When performing ellipsometric analysis, 2 pixels located near the edges of the die were ignored to make sure that the illumination spot corresponding to each analyzed pixel covers identical and enough grating periods (the illumination spot corresponding to a single pixel covers at least 40 grating periods of the etched trench nanostructure in the optimal azimuthal configuration). As can be observed from Fig. 8, there are several nanometer variations in the structural parameters of the etched trench nanostructure over the entire die. But overall, the parameter maps exhibit relatively uniform variation and reasonable agreement with the corresponding result measured by TEM. In conclusion, the results presented in Table 2, Figs. 7 and 8 further demonstrate that we can achieve Mueller matrix measurement and analysis for grating structures with pixel-sized illumination spots by using MMIE. We can also efficiently obtain the parameter maps of grating structures over a wide area with a pixel-sized lateral resolution by performing parallel ellipsometric analysis for all the pixels of interest. In addition, although the MMIE-measured results presented in Tables 1 and 2 were all extracted from the Mueller matrix spectra

#239998 Received 28 Apr 2015; revised 18 Jun 2015; accepted 22 Jun 2015; published 24 Jun 2015
© 2015 OSA

collected by a single pixel of the camera, it is worth pointing out that we can also average the Mueller matrices collected by multiple adjacent pixels to improve the signal to noise ratio for robust grating reconstruction.

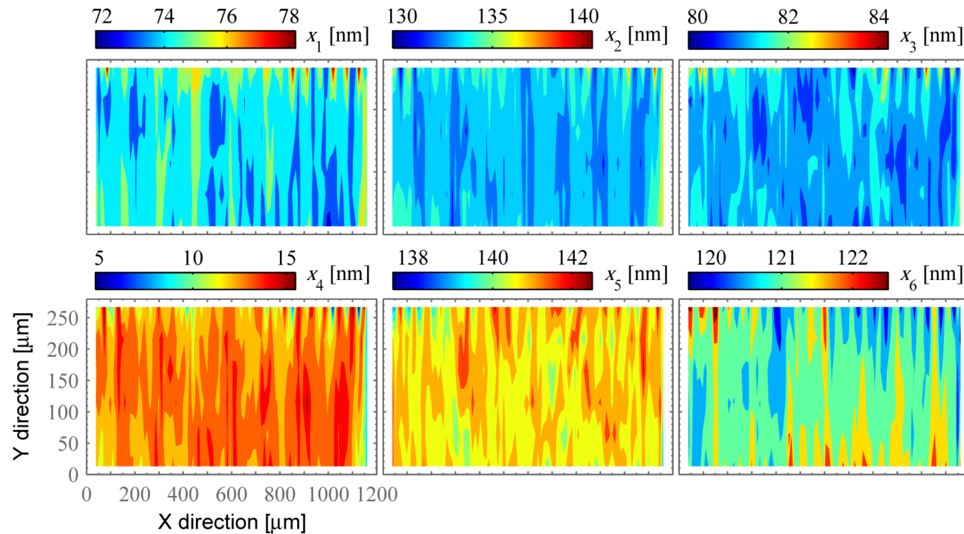

Fig. 8. Maps of the structural parameters x_1~x_6 of the etched trench nanostructure over an entire die. The grating period is along the X direction. Data were obtained by performing ellipsometric analysis for each pixel of the measured imaging Mueller matrices. The measurement configuration is identical to that given in Fig. 7.

5. Conclusions

In this work, MMIE is introduced to reconstruct grating structures. Two kinds of grating structures were measured using an in-house developed Mueller matrix imaging ellipsometer. One is a Si grating structure that is used as a template in nanoimprint lithography, and another one is a typical etched trench nanostructure from the practical manufacturing process lines of flash memory storage cells. The experimental results have demonstrated that MMIE at least has the following three advantages over conventional non-imaging optical scatterometry techniques.

(1) MMIE can acquire a 4 × 4 imaging Mueller matrix in a single measurement, which allows for the direct visualization of the sample and intuitive selection of interested regions for ellipsometric analysis.

(2) We can achieve Mueller matrix measurement and analysis for grating structures with pixel-sized illumination spots, which are much smaller than the microspot sizes in scatterometry techniques.

(3) We can efficiently construct parameter maps of the grating structures over a wide area with pixel-sized lateral resolution by performing parallel ellipsometric analysis for all the pixels of interest without scanning the sample stage as do in scatterometry techniques.

Acknowledgments

This work was funded by the National Natural Science Foundation of China (Grant Nos. 51475191 and 51405172), the National Instrument Development Specific Project of China (Grant No. 2011YQ160002), the China Postdoctoral Science Foundation (Grant No. 2014M560607), and the Program for Changjiang Scholars and Innovative Research Team in University of China (Grant No. IRT13017).

#239998 Received 28 Apr 2015; revised 18 Jun 2015; accepted 22 Jun 2015; published 24 Jun 2015
© 2015 OSA